Electronic Supplementary Material (ESI) for Chemical Communications.


***Supporting information***

# $Ni(OH)_2$-decorated FeCoPi nanosheets on NiO heterostructures: tunable intrinsic electronic structures for improved overall water splitting

*Sundaramoorthy Marimuthu, Ayyavu Shankar and Govindhan Maduraiveeran**

*Materials Electrochemistry Laboratory, Department of Chemistry, College of Engineering and Technology, SRM Institute of Science and Technology, Kattankulathur - 603 203, Chengalpattu District, Tamil Nadu, India*

*Corresponding Author E-mail: *maduraig@srmist.edu.in*

## EXPERIMENTAL SECTION

### Chemicals

Ferric chloride anhydrous ($FeCl_3$), cobalt (II) nitrate hexahydrate ($Co(NO_3)_2.6H_2O$), nickel(II) nitrate hexahydrate ($Ni(NO_3)_2.6H_2O$), and KOH pellets were purchased from Sigma-Aldrich. Nitric acid and sodium hypophosphite were obtained from Alfa-Aesar. All analytical grade chemicals were used exactly as they were obtained. All of the solutions in this investigation were made with pure water (18.2 MΩ cm) collected from a NANO pure Diamond UV deionized water purification system.

### Fabrication of $M(OH)_2@Fe_xCo_{1-x}Pi$ | NiO Heterostructures

Primarily, nickel electrode substrate (geometrical surface area: ~0.8 $cm^2$; dimension of ~0.25 mm radius and ~5.0 mm height) was washed with dilute HCl, ethanol, and deionized water to remove surface oxide and contaminants, and then dried in the air for subsequent use. Firstly, NiO nanostructures were grown on the Ni electrode (NiO | Ni) by chemically pre-treated with 3.0 M nitric acid for 4.0 h.[S1] Secondly, three-dimensional iron-cobalt phosphide nanosheets were electrochemically deposited on nickel oxide nanoparticles by continuous applied potential ($E_{app}$) of 0.1 V vs Ag/AgCl for 40 min using a precursor mixture containing 0.075 M $FeCl_3$ + 0.025 M $Co(NO_3)_2.6H_2O$ + 0.075 M sodium dihydrogen phosphate + 0.1 M $HNO_3$.[S2] Thirdly, $Ni(OH)_2$ was directly electrodeposited on a $Fe_{1-x}Co_xPi$|NiO electrode from 0.1 M Ni $(NO_3)_2.6H_2O$ + 1.0 M KOH aqueous solution at a constant potential of -1.0 V vs Ag/AgCl for 420 s at room temperature.[S3] The developed $Ni(OH)_2$ decorated $Fe_{1-x}Co_xPi$|NiO electrodes are denoted as $Ni(OH)_2@Fe_xCo_{1-x}Pi$|NiO. For the comparison, other transition metal double hydroxides ($Ni(OH)_2$, $Fe(OH)_2$,

$Co(OH)_2$, and $Cu(OH)_2$) were prepared using of similar experimental settings. They are described as $Fe(OH)_2@Fe_xCo_{1-x}Pi|NiO$, $Co(OH)_2@Fe_xCo_{1-x}Pi|NiO$ and $Cu(OH)_2@Fe_xCo_{1-x}Pi|NiO$ heterostructures throughout the study. The electrodes were then washed with deionized water, and dried in the air for electrochemical water splitting study.

**Characterization**

Primarily, high resolution scanning electron microscope (HR-SEM) (Thermosceintific Apreo S) equipped with EDS (FEI QUANTA 200 with an accelerating voltage of 20 kV) was utilized for studying surface morphology, elemental composition and elemental mapping of the electrodes. Transmission electron microscopic (TEM) and high-resolution transmission electron microscopic (HRTEM) studies were conducted with a JEOL 2010F TEM. X-ray diffraction (XRD) analysis were performed by using a PANanalyticalXpert Pro diffractometer with a Ni filtered monochromatic Cu Kr (1.5406 Å, 2.2 KW Max). X-ray photoelectron spectroscopic (XPS) studies were employed with a-PHI Versaprobe III to understand the chemical state and composition of the catalysts.

All electrochemical experiments were conducted using standard three electrode cells, with Ag/AgCl (3.0 KCl) employed as the reference electrode, the platinum coil served as the counter electrode, and the nickel electrode acted as the working electrode. The EIS test was used to investigate the kinetics of the OER process in the frequency range of 1 kHz - 100 MHz with different applied potentials. The electrochemical impedance data was fitted using EC lab software. The following equation was used to convert all voltages to ($E_{(RHE)} = E_{(Ag/AgCl)} + 0.059\ pH + E^0$, where $E^0 = 0.197$ V at 25 °C). The mass loading m (g $cm^2$) of the catalysts and the measured current density $j$ (A $cm^2$) at different overpotential (mass activity = j/m) were used to calculate the mass activity value (A $g^{-1}$).[S4]

The electrochemical active surface area (ECSA) of the as-developed electrodes was calculated using double-layer capacitance ($C_{dl}$) and specific capacitance ($C_S$) is 11.57 mF $cm^{-2}$, both of which were measured using cyclic voltammetry (CV) at different scan rates, starting from 10 to 125 mV $s^{-1}$.[S5]

$$ECSA = C_{dl} / C_S \quad (1)$$

The Turn over frequency (TOF) was calculated using of Eqn. (2) and (3).[S6]

$$n = m_{mass} / M \quad (2)$$

$$TOF = JA / 4Fn \quad (3)$$

where "n" is the number of moles of the active sites, "$m_{mass}$" means catalyst loading, and "M" represents molar mass of catalysts. "$J$" describes the current density at overpotential ($\eta$) of ~0.133 V in A $cm^{-2}$, "A" means surface area of the nickel substrate (~0.81 $cm^2$), "F" represents the Faraday constant (96485 C $mol^{-1}$), respectively.

Significantly, the incorporation of $Ni(OH)_2$ further reduced the overpotential with higher electrocatalytic activity towards the water splitting in comparison to other $Co(OH)_2$, $Cu(OH)_2$, $Fe(OH)_2$ and FeCoPi, as displayed in Figs. 1(a and b), S12 and S13, due to the following attributes: Firstly, the active $Ni(OH)_2$ nanosheets can provide added catalytic active sites during OER; Secondly, the strong electronic interaction among the constituents can aid in improving the charge-transfer process; and Thirdly, the interfacial region may further stabilize the surface of the catalysts for the adsorption of water reactants/intermediates, lowering the sluggish energy barriers in the primary phases.

The as-developed $Ni(OH)_2@Fe_xCo_{1-x}Pi|NiO$ heterostructures possess reduced free energy change for the formation of HOO* intermediates (rate-limiting step) in OER, suggesting the

energetically favorable adsorption of HOO* intermediates on the surface, and accelerate the electrode kinetics, as supported by the experimental study (Figs. S12 and S13). On the other hand, A reactant water molecules strongly adsorbed at the interface of the $Ni(OH)_2@Fe_xCo_{1-x}Pi|NiO$ heterostructures in the Volmer step of HER, and dissociated into $OH^-$ and H*. The H* successively adsorbed on the local FeCoPi sites whereas the OH- chemisorbed on the surface of $Ni(OH)_2$, facilitating the generation of $H_2$ gas. The water dissociation, chemisorption of $OH^-$ and the strong electronic interaction of $Ni(OH)_2$ with FeCoPi can thus accelerate HER activity and kinetics under alkaline electrolyte (Figs. 3, S20 and S21).

The strong electronic interaction of among the $Ni(OH)_2$ and FeCoPi materials pays for reinforcing the interfacial reactivity of the catalysts. The $Ni(OH)_2@Fe_xCo_{1-x}Pi|NiO$ heterostructures accelerate the charge-transfer process and improving the active sites with stabilizing the HOO* intermediates, promoting the rate-determining HOO* step during OER. It also stimulates the adsorption of water molecules and chemisorption of H* intermediates in HER with the aid of $Ni(OH)_2$, facilitating the rate-limiting Volmer-step. Thereby, the bifunctional $Ni(OH)_2@Fe_xCo_{1-x}Pi|NiO$ catalysts enable water electrolysis at low cell voltage with good durability (Figs. S18, S19, 3(b), S23, and Fig. 3(d)).

**Table S1.** List of the developed $M(OH)_2@Fe_xCo_{1-x}Pi|NiO$ electrodes and their electrocatalytic OER performance.

| S. No | Electrodes | $E_{onset}$ / V (RHE) | $\eta_{OER}$ (mV) @ 10 mA cm$^{-2}$ |
|---|---|---|---|
| 1 | 3D- $Ni(OH)_2@Fe_xCo_{1-x}Pi|NiO$ | 1.34 | 133 |
| 2 | 3D- $Fe(OH)_2@Fe_xCo_{1-x}Pi|NiO$ | 1.42 | 222 |
| 3 | 3D- $Co(OH)_2@Fe_xCo_{1-x}Pi|NiO$ | 1.46 | 269 |
| 4 | 3D- $Cu(OH)_2@Fe_xCo_{1-x}Pi|NiO$ | 1.39 | 207 |
| 5 | 3D-$Fe_{1-x}Co_xP$-A NS@NiO NPs | 1.35 | 158 |
| 6 | 3D-$Ni(OH)_2$@NiO | 1.36 | 169 |
| 7 | $Ni(OH)_2@Fe_xCo_{1-x}Pi|CuO$ | 1.43 | 233 |
| 8 | $Ni(OH)_2@Fe_xCo_{1-x}Pi|SS$ | 1.34 | 139 |
| 9 | Commercial $IrO_2$ | 1.53 | 337 |
| Pi: Phosphides; SS: Stainless Steel; Cu: Copper; Ni- Nickel electrode | | | |

**Table S2.** Comparison of the OER and HER performance of the $Ni(OH)_2@Fe_xCo_{1-x}Pi|NiO$ heterostructures with the recently reported catalysts in the literature.

| S. No | Materials | Synthetic method | Overpotential ($\eta$) (mV) OER | Overpotential ($\eta$) (mV) HER | Current Density (mA $cm^{-2}$) | Ref |
|---|---|---|---|---|---|---|
| 1 | CoFe-P/NF | Electrodeposition | 287 | 45 | 10 | S7 |
| 2 | $Ni(OH)_2$-$Fe_2P$/TM | Electrodeposition | - | 76 | 10 | S8 |
| 3 | $Ni(OH)_2/Ni_3S_2$ | co-precipitation and sulfuration | 270 | 211 | 20 | S9 |
| 4 | $Ni(OH)_2$/NF | Electrodeposition | 166 | 187 | 20 | S10 |
| 5 | $Ni_3S_2/Ni(OH)_2$-NF | Electrodeposition | 249 | 66 | 20 & 10 | S11 |
| 6 | $Ni(OH)_2$/NF | hydrothermal | 330 | 172 | 50 & 20 | S12 |
| 7 | $Ni(OH)_2/NiCo_2O_4$ | hydrothermal | 224 | 189 | 10 | S13 |
| 8 | NiFeCoPi/P | Electrodeposition | 299 | 98 | 10 | S14 |
| 9 | FeSe/$Co_2P$/NF | Solvothermal and Electrodeposition | 235 & 265 | - | 10 & 50 | S15 |
| 10 | PS-3D-FeP@NiO\|Ni | Electrodeposition | 170 | - | 10 | S16 |
| 11 | 3D-$Fe_{1-x}Co_xP$-A NS@NiO NPs\|Ni | Electrodeposition | 158 | 74 | 10 | S2 |
| **12** | **$Ni(OH)_2@Fe_xCo_{1-x}Pi|NiO$** | **Electrodeposition** | **133** | **171** | **10** | **This Study** |

TM-Ti mesh; CC- Carbon cloth; NF- Nickel foam;

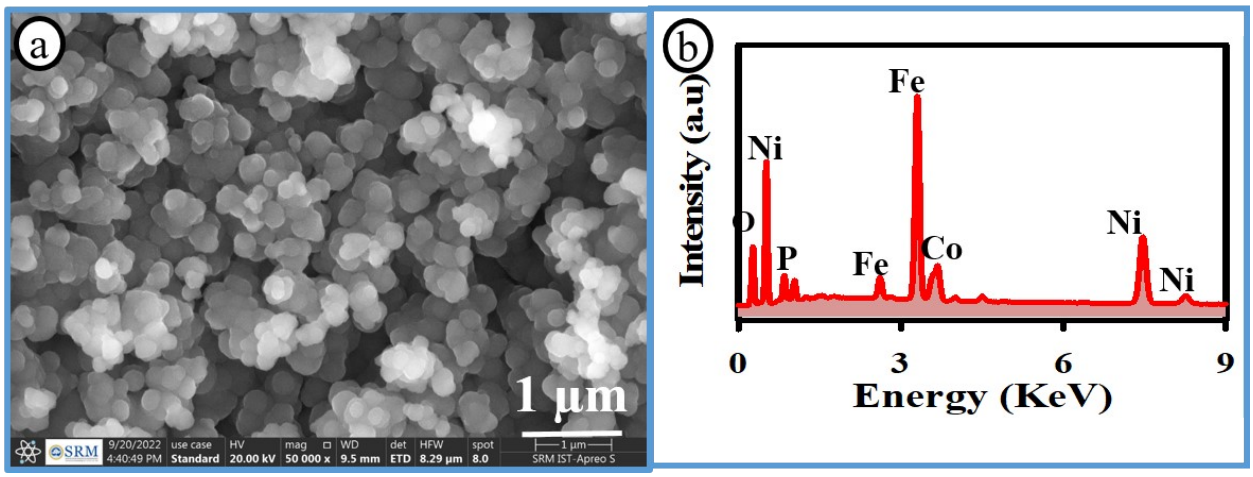


**Fig. S1.** HRSEM image (a), and EDX spectra (b) of the $Ni(OH)_2@Fe_xCo_{1-x}Pi|NiO$ heterostructures.

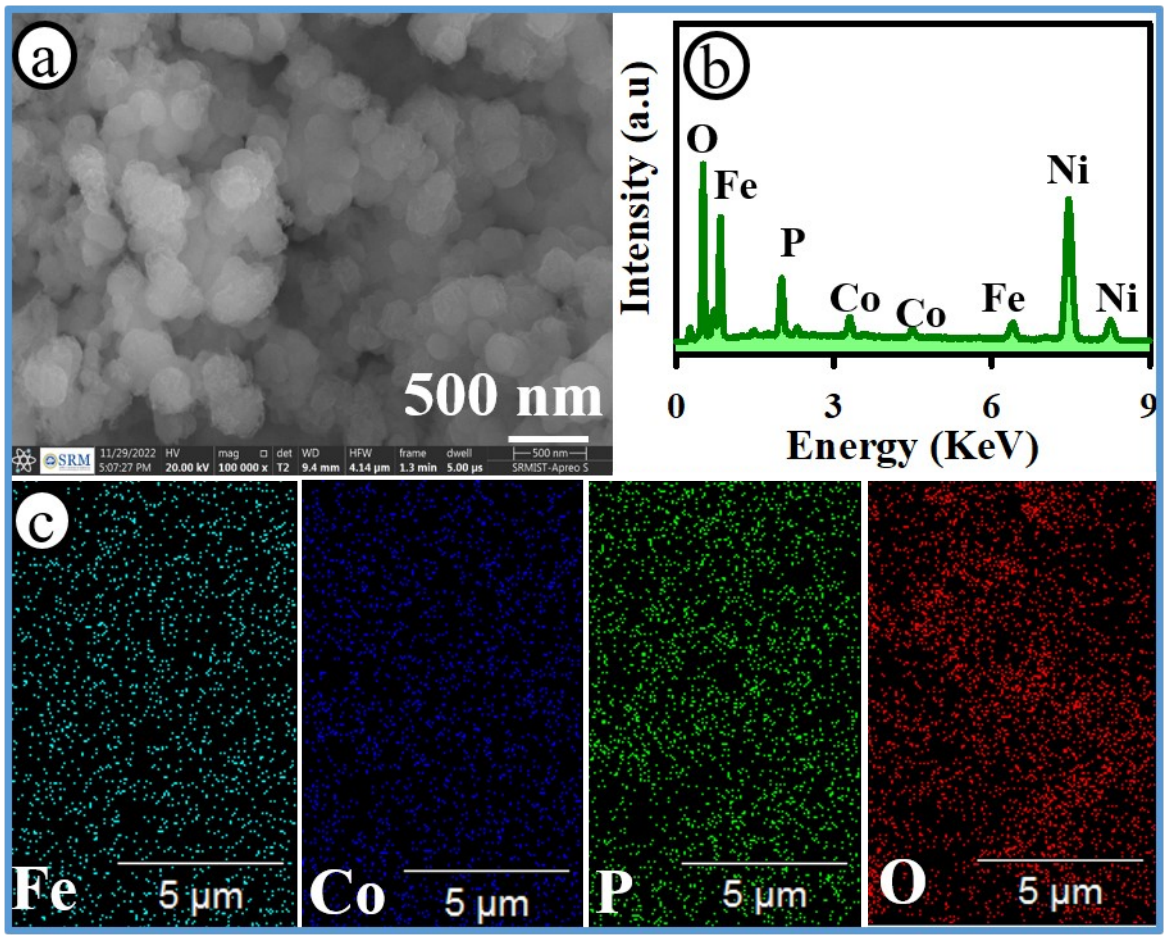


**Fig. S2.** SEM image (a), EDX spectra (b) and elemental mapping of Fe, Co, P and O (c) for the $Fe(OH)_2@Fe_xCo_{1-x}Pi|NiO$ heterostructures.

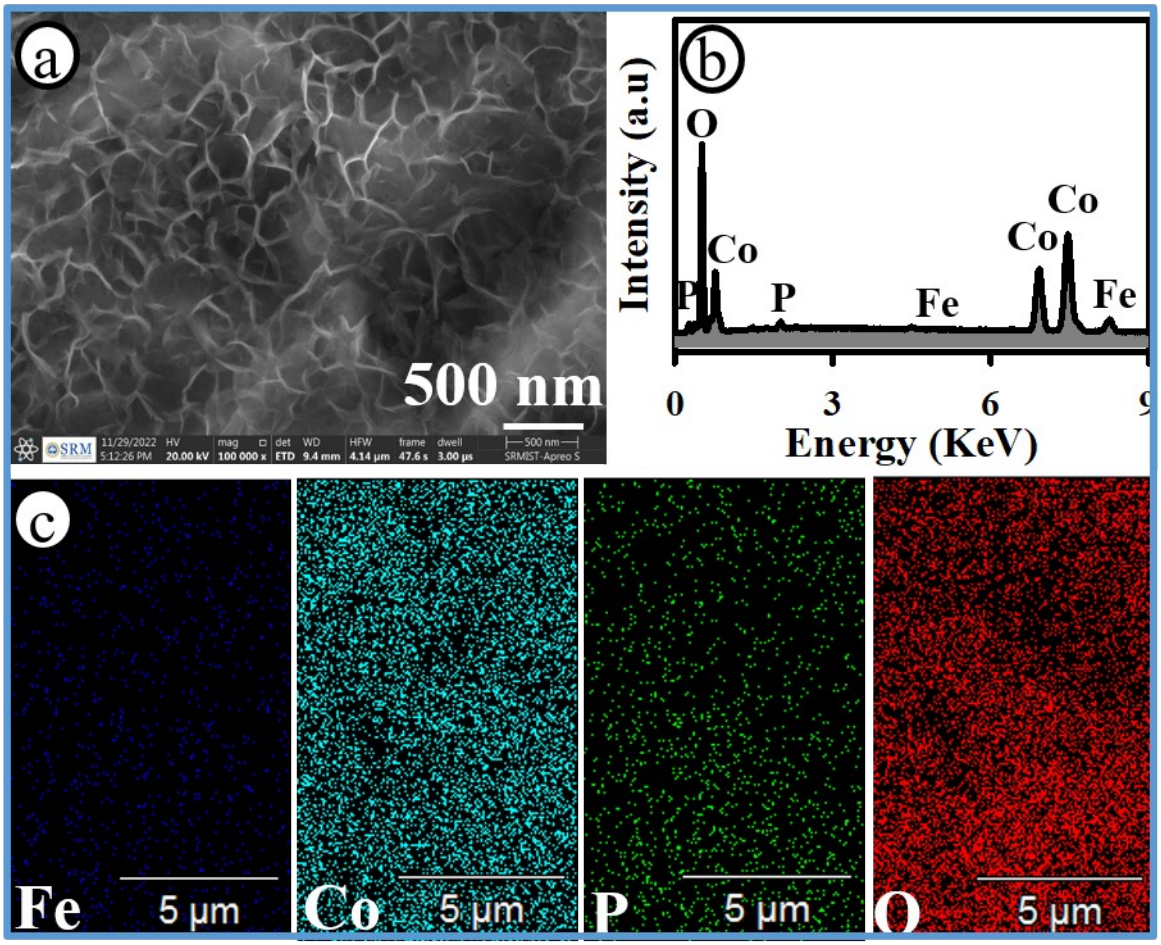


**Fig. S3.** SEM image (a), EDX spectra (b) and elemental mapping of Fe, Co, P and O (c) for the $Co(OH)_2@Fe_xCo_{1-x}Pi|NiO$ heterostructures.

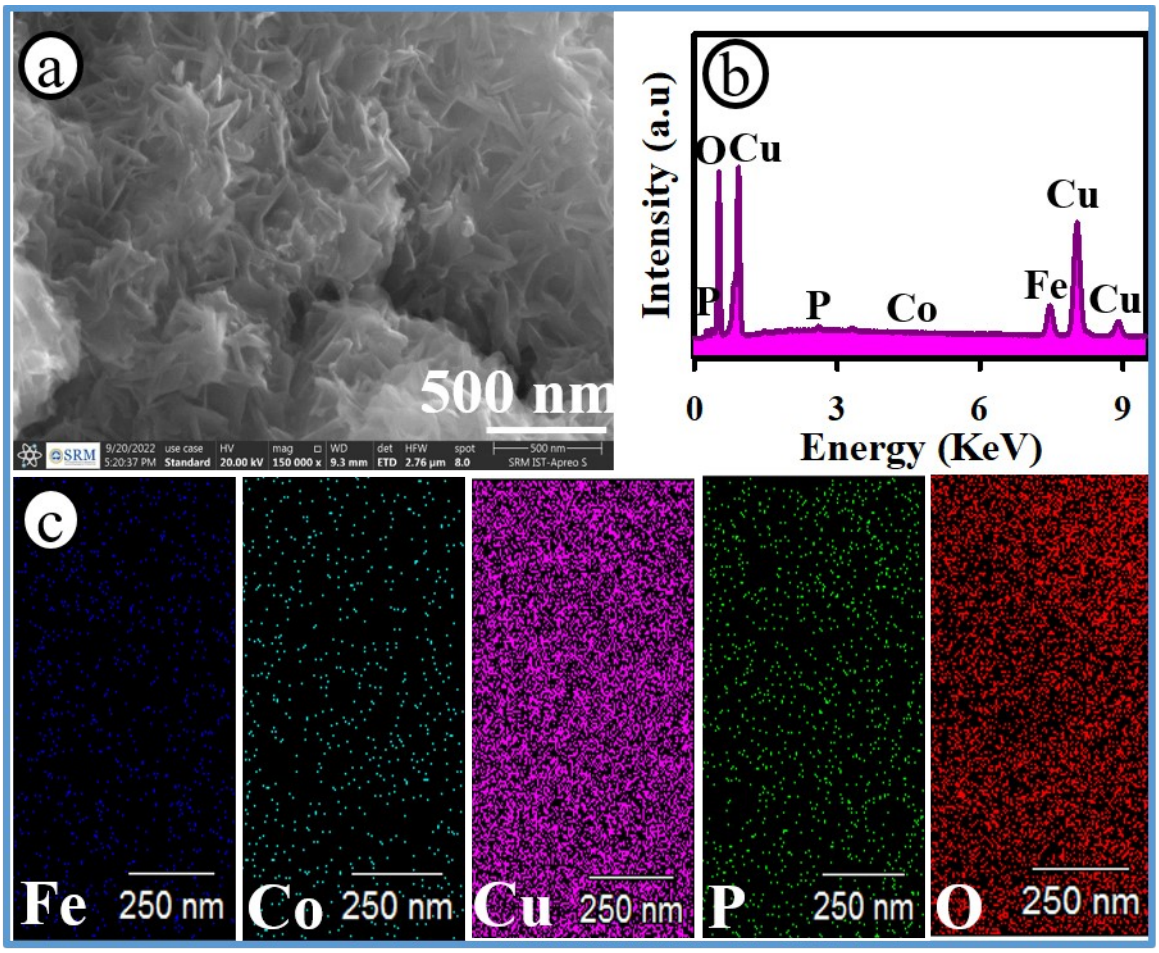


**Fig. S4.** SEM image (a), EDX spectra (b) and elemental mapping of Fe, Co, Cu, P and O (c) for the $Cu(OH)_2@Fe_xCo_{1-x}Pi|NiO$ heterostructures.

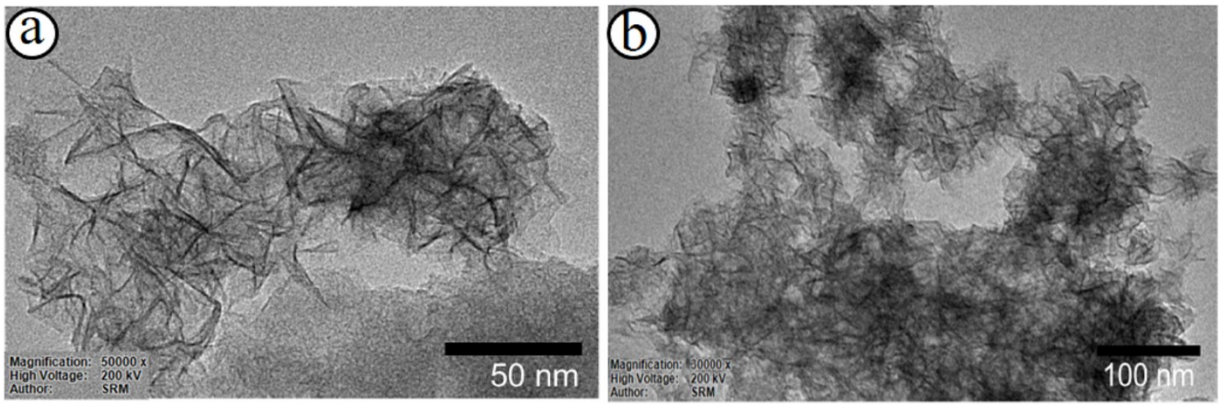


**Fig. S5.** TEM images of the $Ni(OH)_2@Fe_xCo_{1-x}Pi|NiO$ heterostructures with high (a) and low resolution (b).

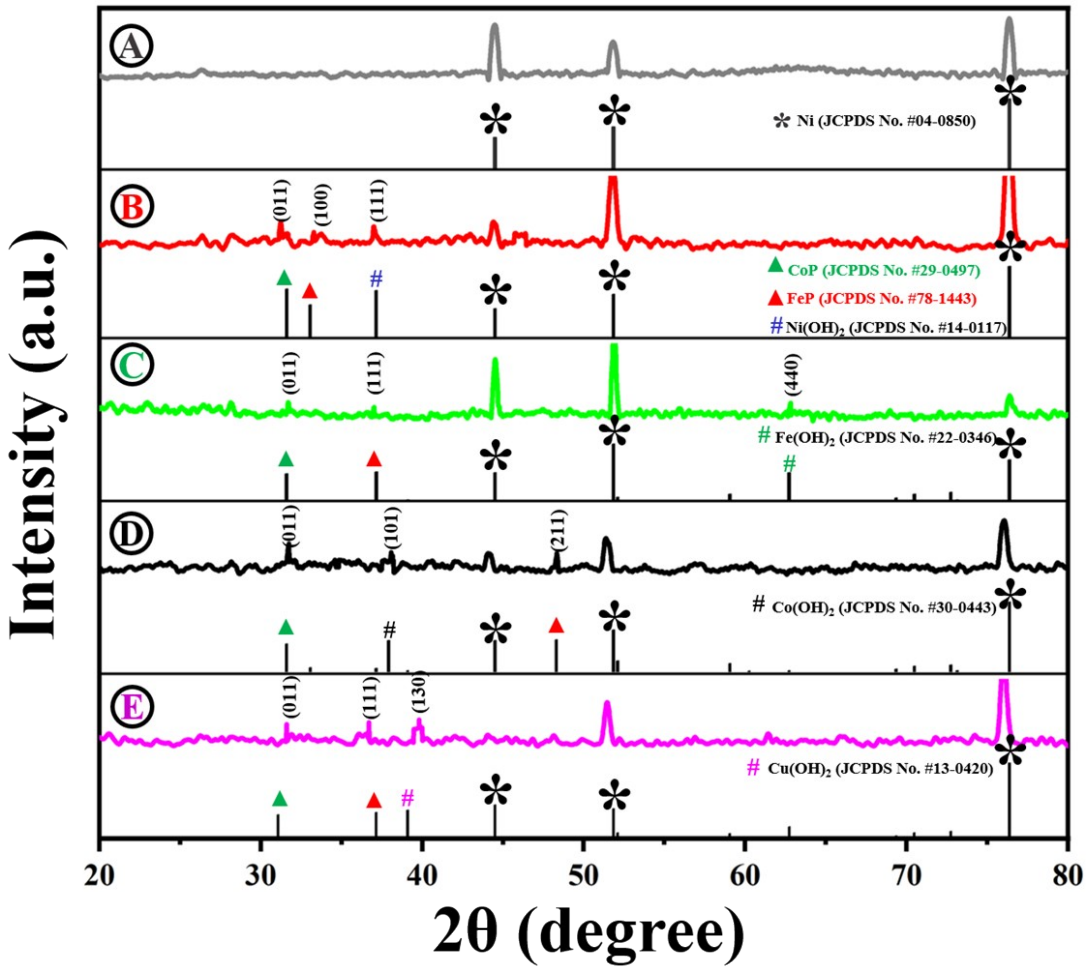


**Fig. S6.** XRD pattern of the bare Ni (grey, (A)), $Ni(OH)_2@Fe_xCo_{1-x}Pi|NiO$ (red, (B)), $Fe(OH)_2@Fe_xCo_{1-x}Pi|NiO$ (green, (C)), $Co(OH)_2@Fe_xCo_{1-x}Pi|NiO$ (black, (D)) and $Cu(OH)_2@Fe_xCo_{1-x}Pi|NiO$ (violet, (E)) heterostructured electrodes, where (*)-marked peaks corresponded to Ni substrate.

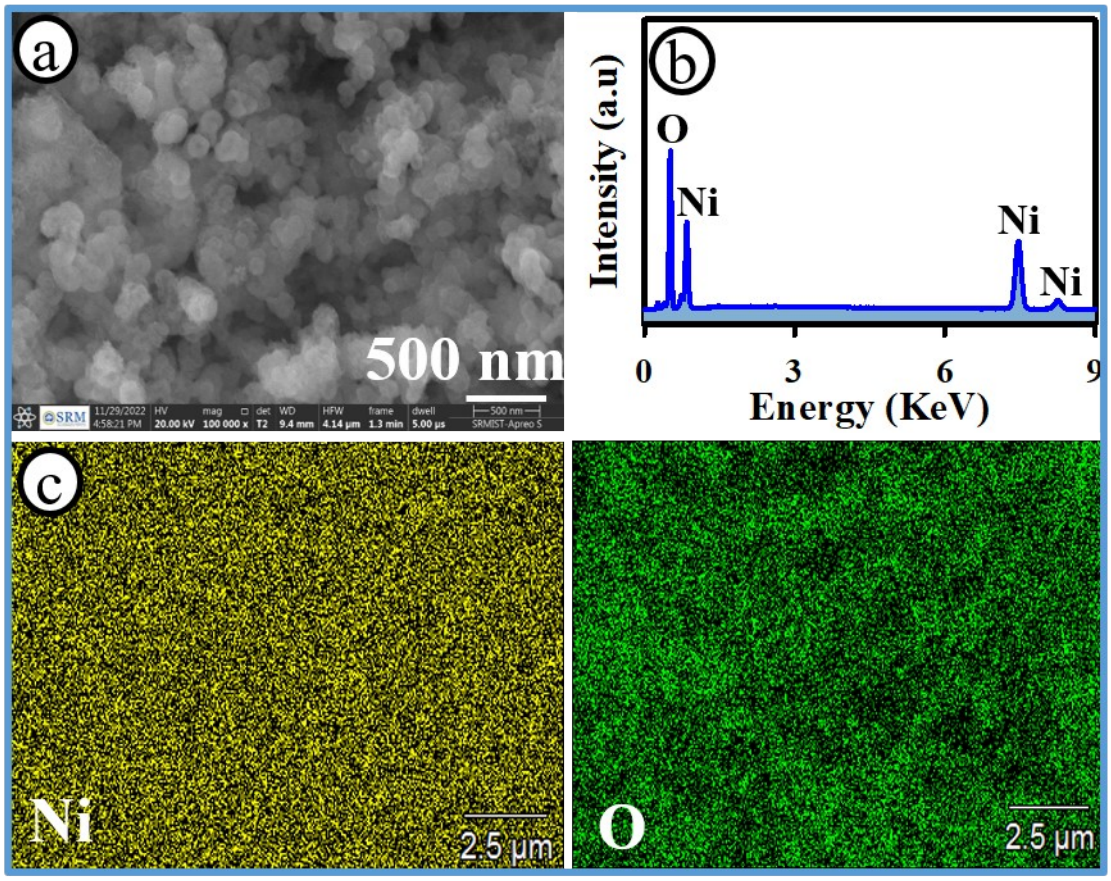


**Fig. S7.** SEM image (a), EDX spectra (b) and elemental mapping of Ni and O (c) for the 3D-$Ni(OH)_2$@NiO electrode.

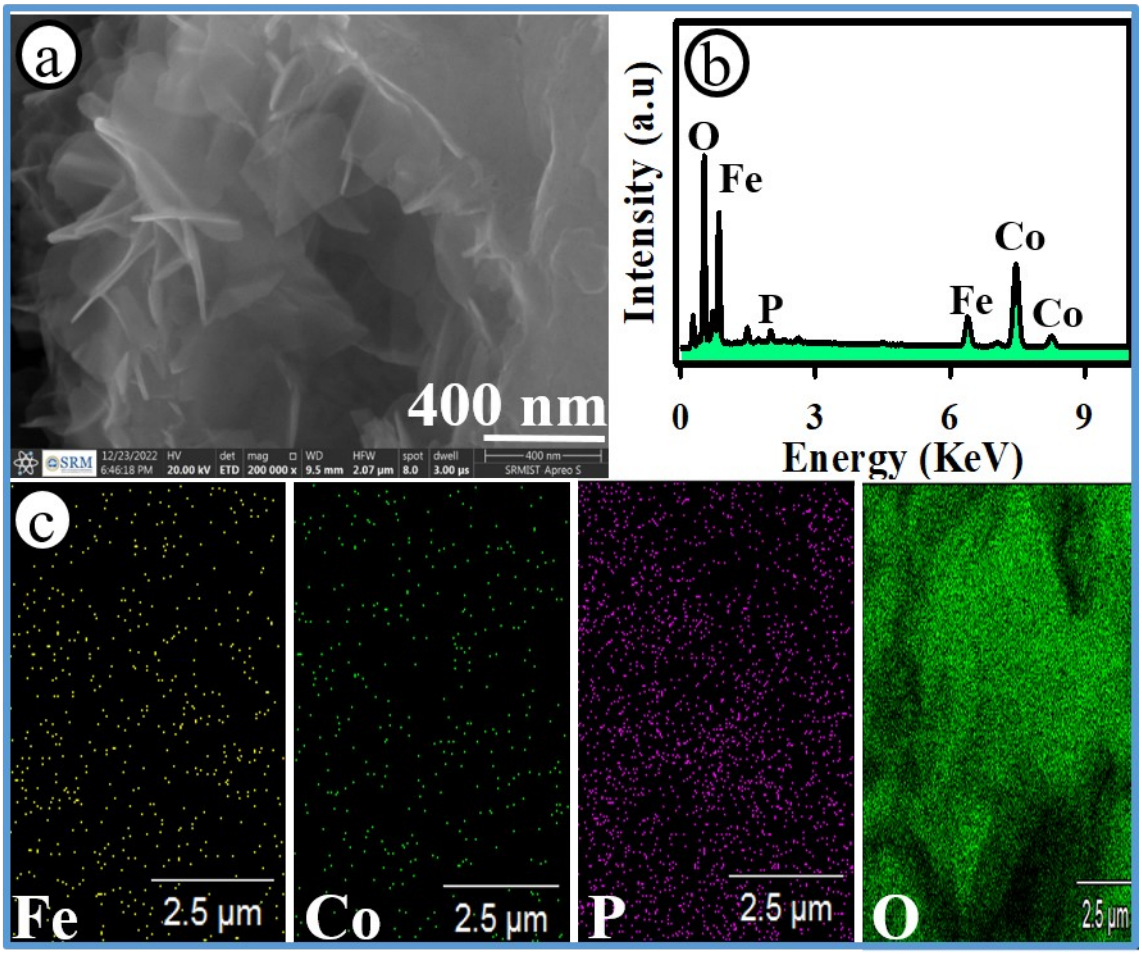


**Fig. S8.** SEM image (a), EDX spectra (b) and elemental mapping of Fe, Co, P and O (c) for the $Fe_xCo_{1-x}Pi|NiO$ heterostructures.

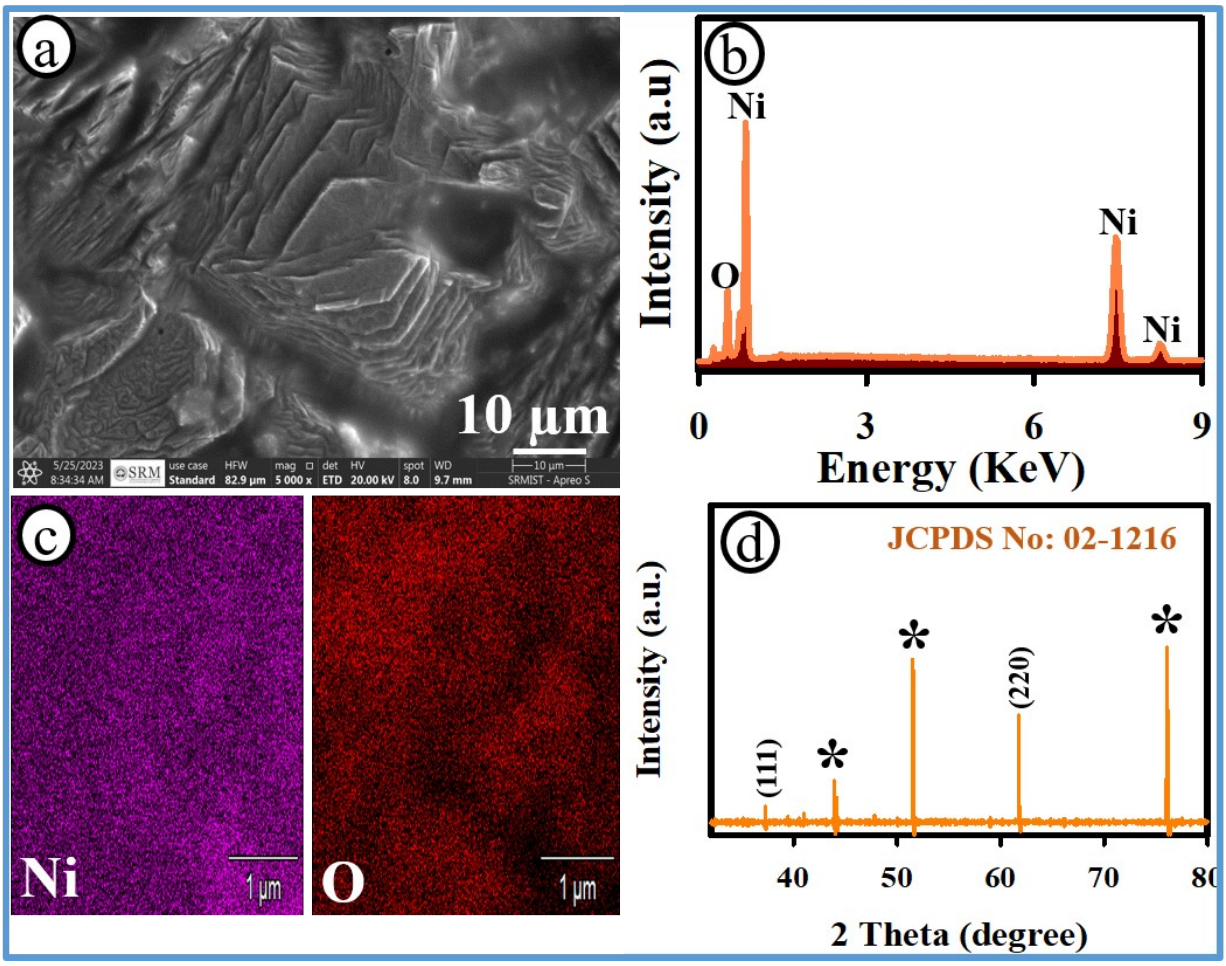


**Fig. S9.** HRSEM image (a), EDX spectra (b) and elemental mapping of Ni and O (c) and XRD pattern of NiO (d) for the NiO NPs|Ni electrode, where (*)-marked peaks corresponded to Ni substrate.

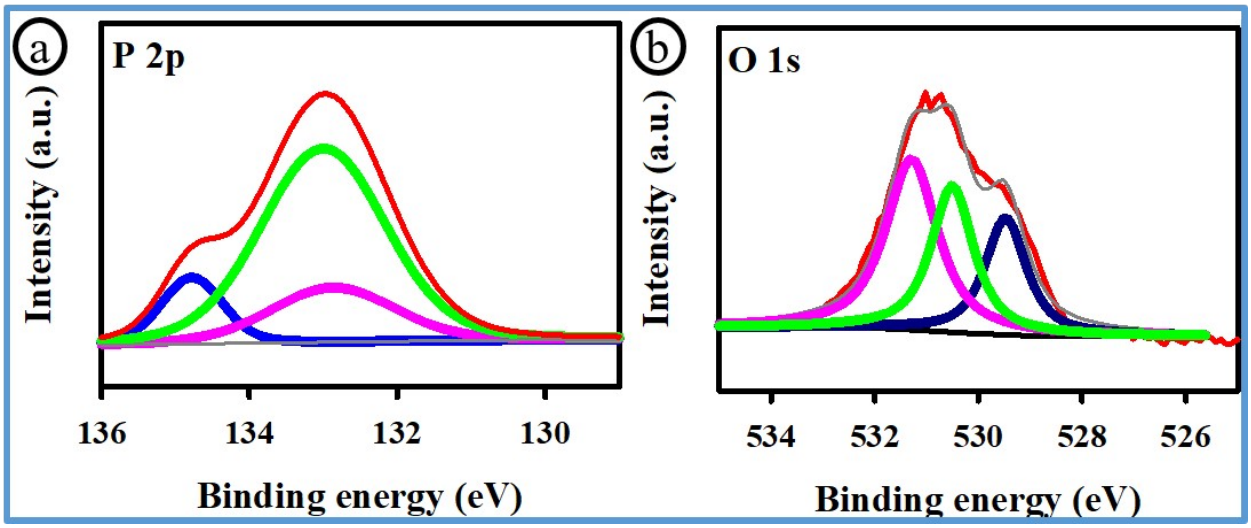


**Fig. S10.** XPS spectra P 2p (a), and O 1s (b) of the $Ni(OH)_2@Fe_xCo_{1-x}Pi|NiO$ heterostructures.

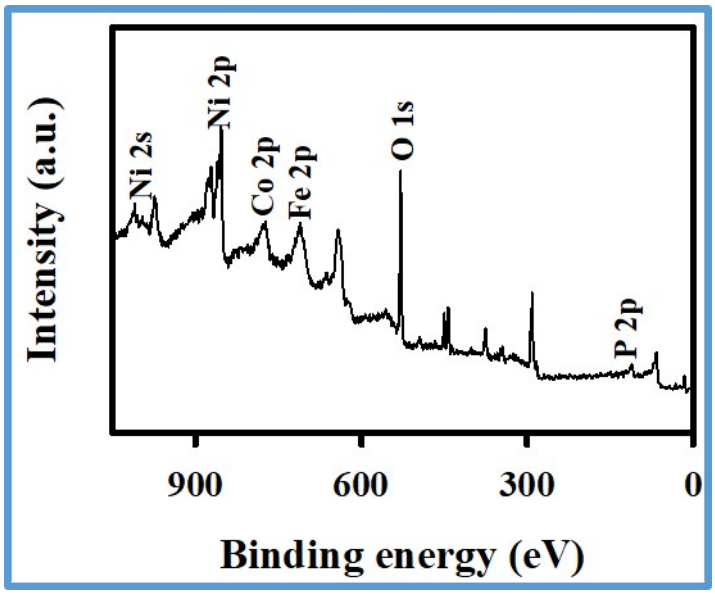


**Fig. S11.** XPS survey spectra of the $Ni(OH)_2@Fe_xCo_{1-x}Pi|NiO$ heterostructures.

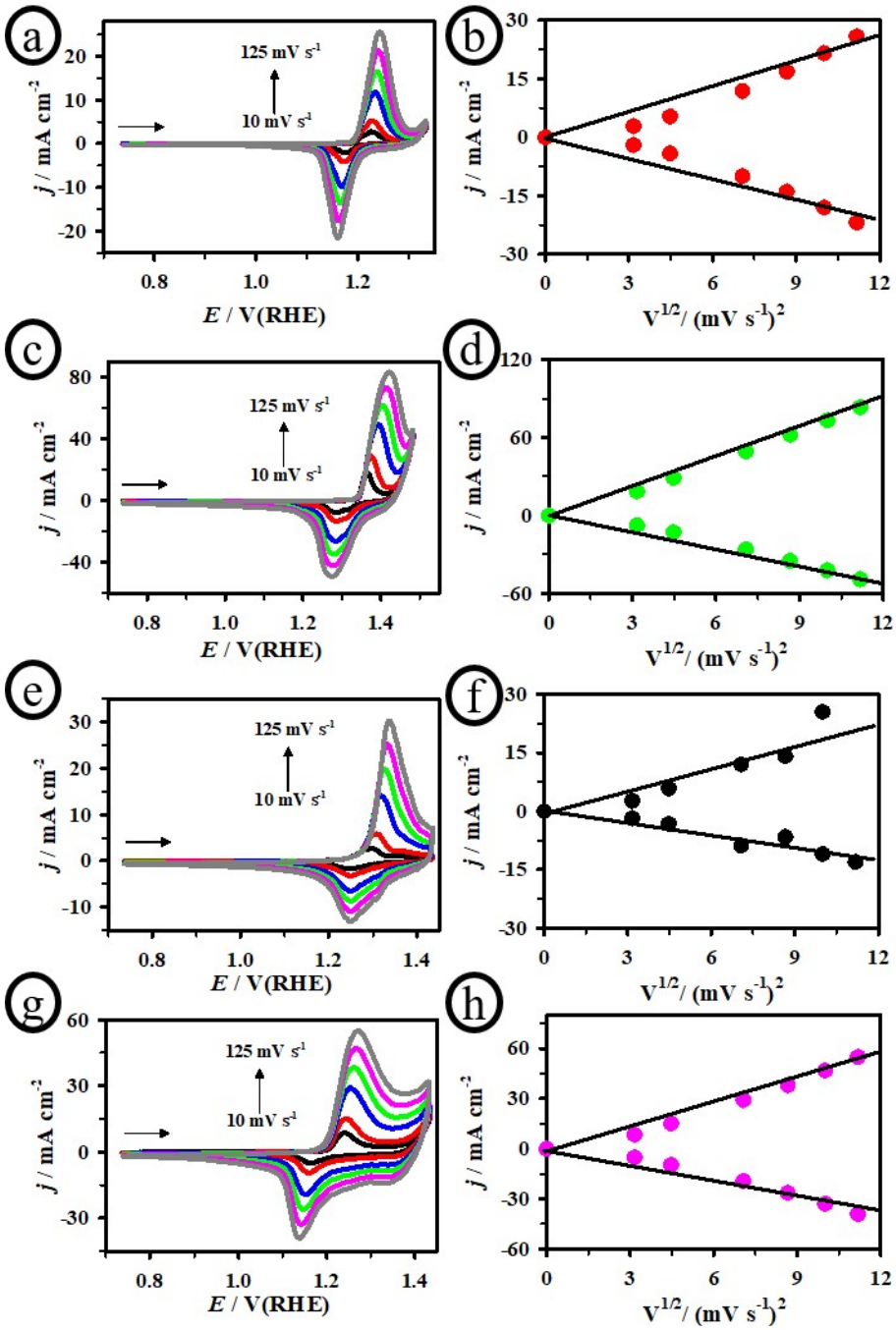


**Fig. S12.** CV curves $Ni(OH)_2@Fe_xCo_{1-x}Pi|NiO$ (a), $Fe(OH)_2@Fe_xCo_{1-x}Pi|NiO$ (c), $Co(OH)_2@Fe_xCo_{1-x}Pi|NiO$ (e) and $Cu(OH)_2@Fe_xCo_{1-x}Pi|NiO$ Ni (g) heterostructures at different scan rates recorded in 1.0 M KOH, starting from 10 to 125 mV $s^{-1}$, and the corresponding plot of peak current density vs square root of the scan rate.

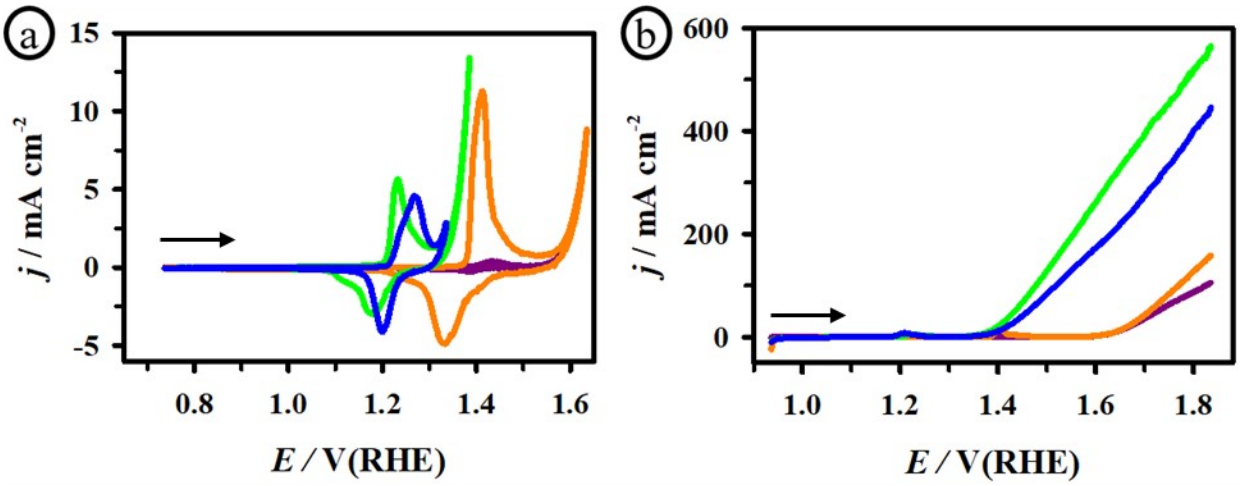


**Fig. S13**. CV (a), and LSV (b) curves of the bare Ni electrode (violet), NiO NPs (orange), $Ni(OH)_2$ @NiO NPs (blue) and $Ni(OH)_2$@$Fe_xCo_{1-x}$Pi|NiO heterostructures (green) recorded in 1.0 KOH at the scan rate of 10.0 $mVs^{-1}$.

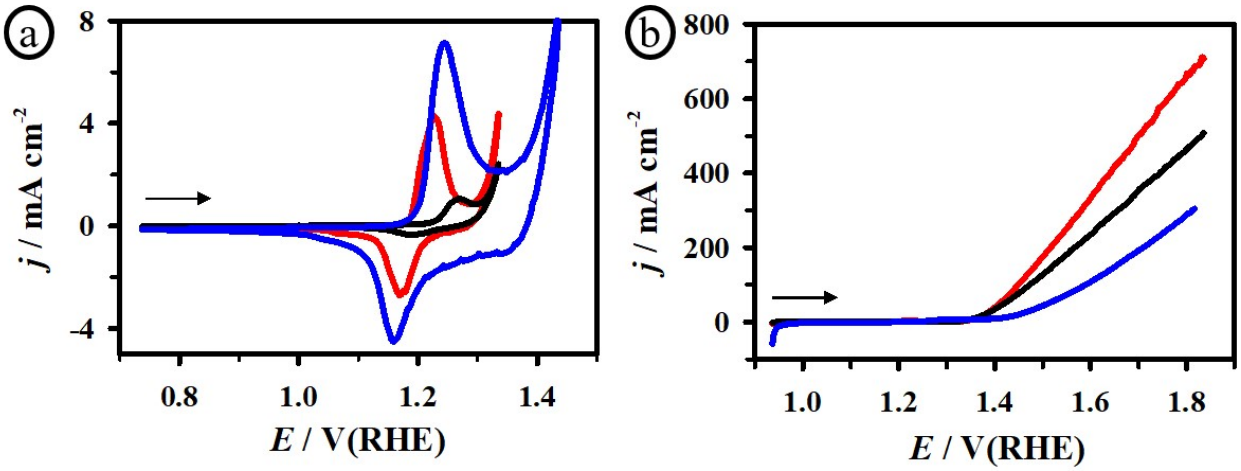


**Fig. S14**. CV (a) and LSV (b) curves of the $Ni(OH)_2@Fe_xCo_{1-x}Pi|CuO$ (blue), $Ni(OH)_2@Fe_xCo_{1-x}Pi|SS$ (black), and $Ni(OH)_2@Fe_xCo_{1-x}Pi|NiO$ (red) heterostructures recorded in 1.0 KOH.

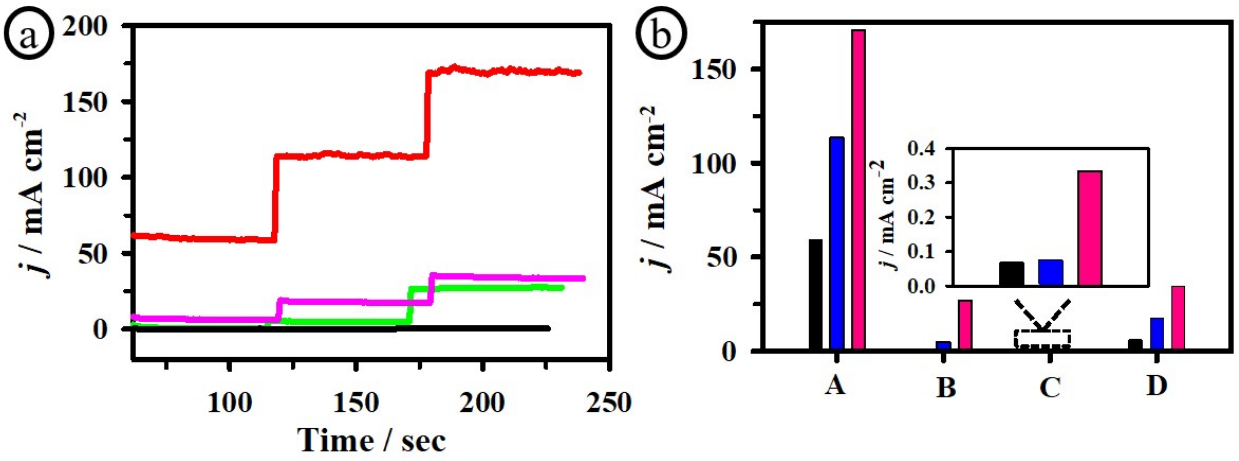


**Fig. S15.** Chronoamperometric response (a), and plot of current density vs various electrodes (b) of $Ni(OH)_2@Fe_xCo_{1-x}Pi|NiO$ (red, (A)), $Fe(OH)_2@Fe_xCo_{1-x}Pi|NiO$ (pink, (B)), $Co(OH)_2@Fe_xCo_{1-x}Pi|NiO$ (green, (C)) and $Cu(OH)_2@Fe_xCo_{1-x}Pi|NiO$ (black, (D)) at different $E_{apps}$ of 1.40 (dark red), 1.44 (dark pink), and 1.48 V (green) vs RHE.

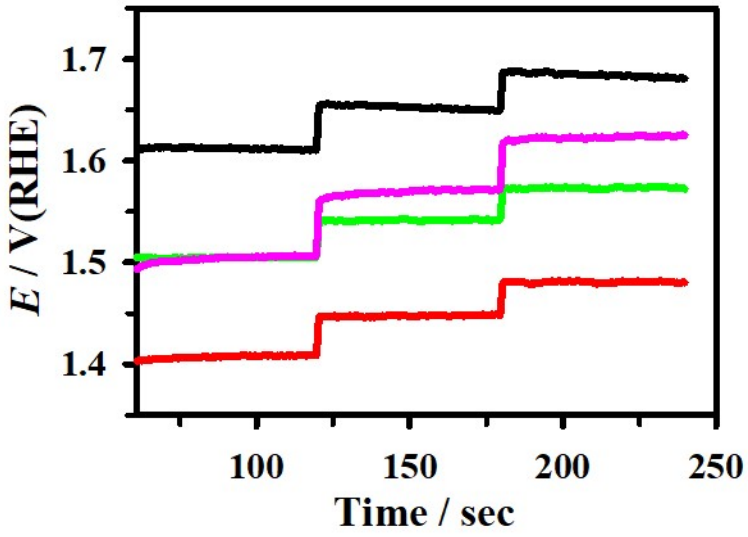


**Fig. S16.** (a) Chronopotentiometric response of the the $Ni(OH)_2@Fe_xCo_{1-x}Pi|NiO$ (red, (A)), $Fe(OH)_2@Fe_xCo_{1-x}Pi|NiO$ (pink, (B)), $Co(OH)_2@Fe_xCo_{1-x}Pi|NiO$ (green, (C)), and $Cu(OH)_2@Fe_xCo_{1-x}Pi|NiO$ (black, (D)) heterostructures at different applied current densities of 50, 100, and 150 mA $cm^{-2}$.

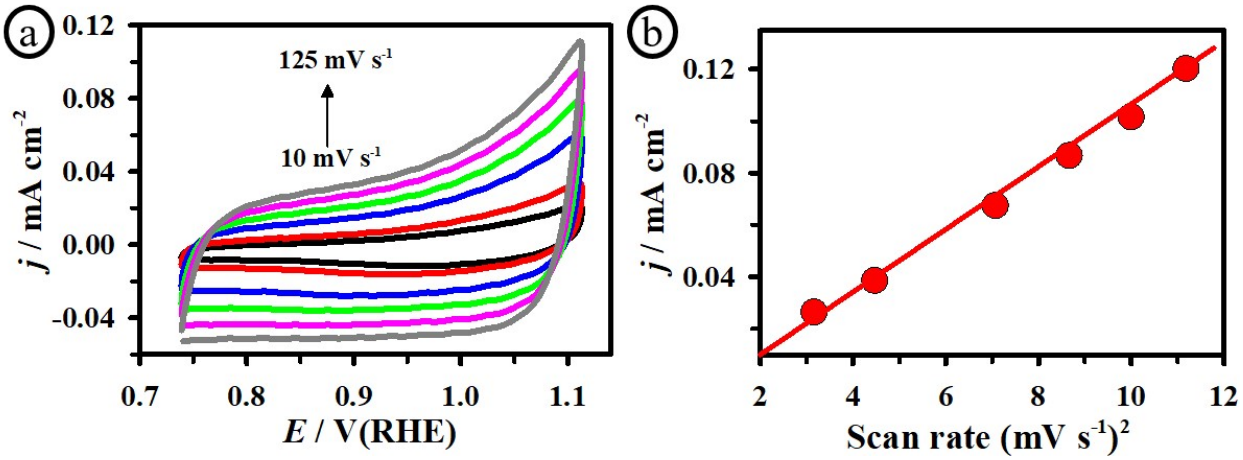


**Fig. S17.** CV curves of the $Ni(OH)_2@Fe_xCo_{1-x}Pi|NiO$ heterostructures recorded in 1.0 M KOH solution at different scan rates from 10 to 125 mV $s^{-1}$ (a). The corresponding plot of non-faradaic anodic current density vs scan rates (b).

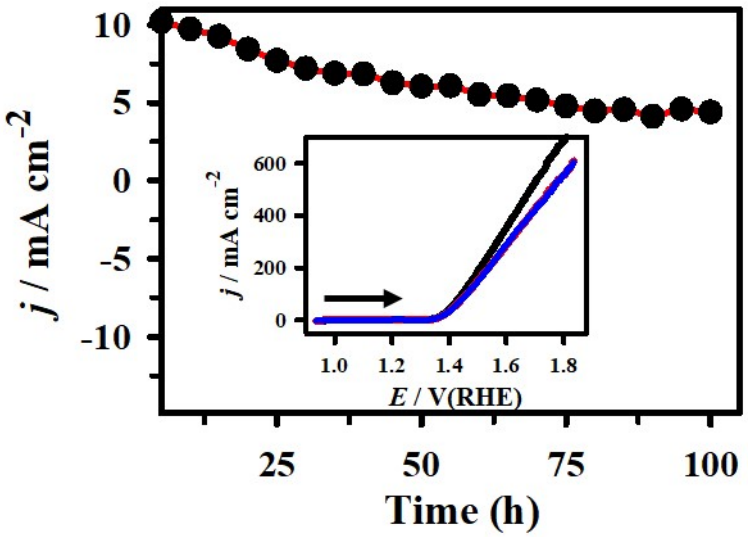


**Fig. S18.** Chronoamperometric response of the $Ni(OH)_2@Fe_xCo_{1-x}Pi|NiO$ heterostructures at the applied constant potential of 1.37 V for 100 h. Inset: LSV curves of three-brand new electrodes of $Ni(OH)_2@Fe_xCo_{1-x}Pi|NiO$ heterostructures recorded in 1.0 M KOH at a scan rate of 10 mV $s^{-1}$.

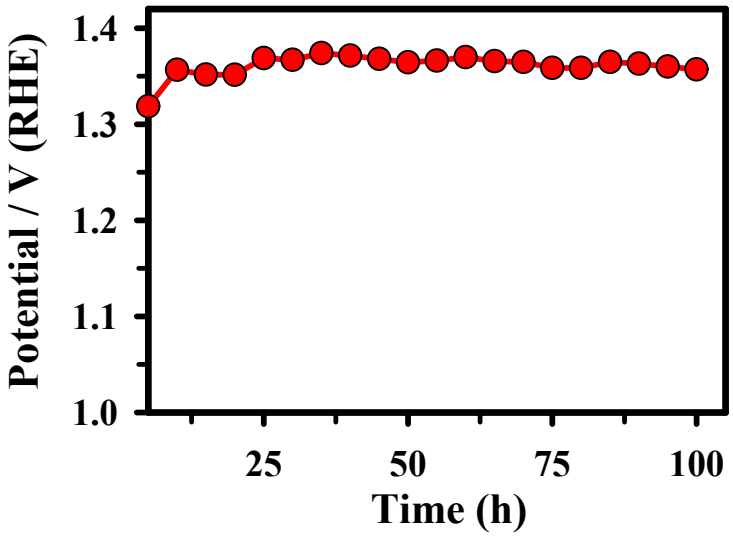


**Fig. S19.** Chronopotentiometric response of the $Ni(OH)_2@Fe_xCo_{1-x}Pi|NiO$ heterostructures at the applied constant current density of 10.0 mA $cm^{-2}$ for 100 h.

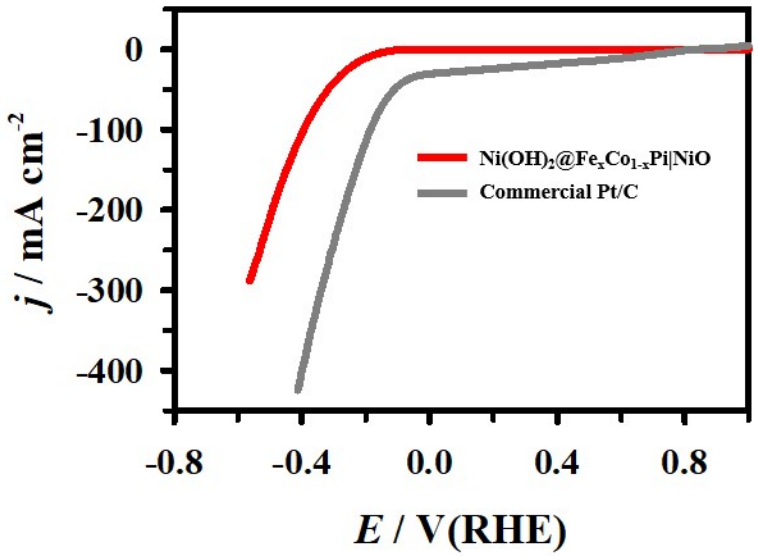


**Fig. S20**. HER polarization curves of $Ni(OH)_2@Fe_xCo_{1-x}Pi|NiO$ heterostructures (red) and commercial Pt/C (grey) electrodes recorded in 1.0 KOH at the scan rate of 10.0 $mVs^{-1}$.

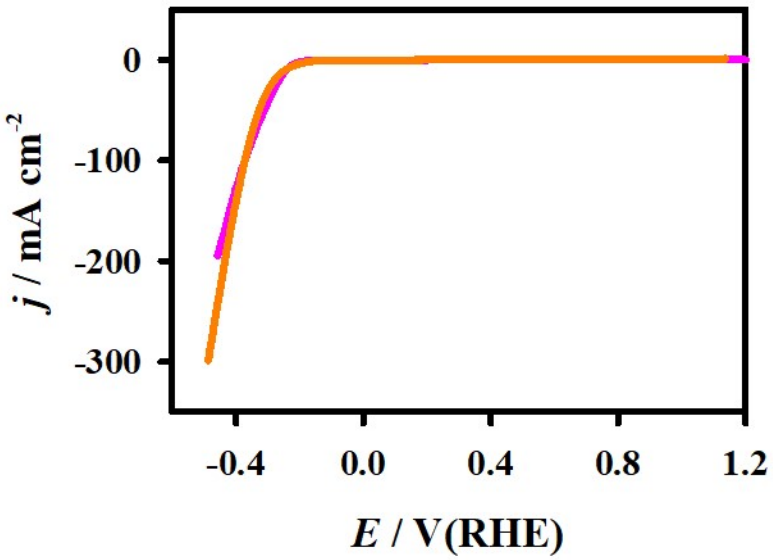


**Fig. S21**. LSV curve of the bare Ni electrode (pink) and NiO NPs|Ni (orange) recorded in 1.0 KOH.

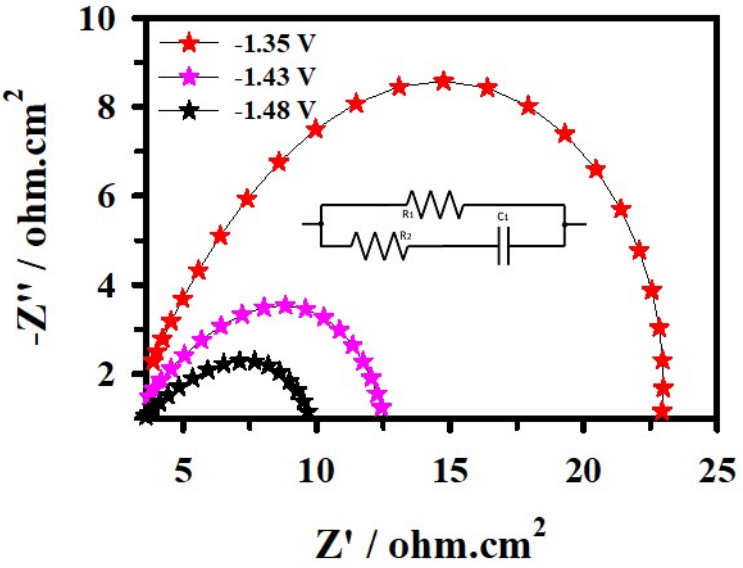


**Fig. S22.** Electrochemical impedence response of the $Ni(OH)_2@Fe_xCo_{1-x}Pi|NiO$ heterostructures at different applied potentials of -1.35 (red), -1.43 (pink) and -1.48 V (black).

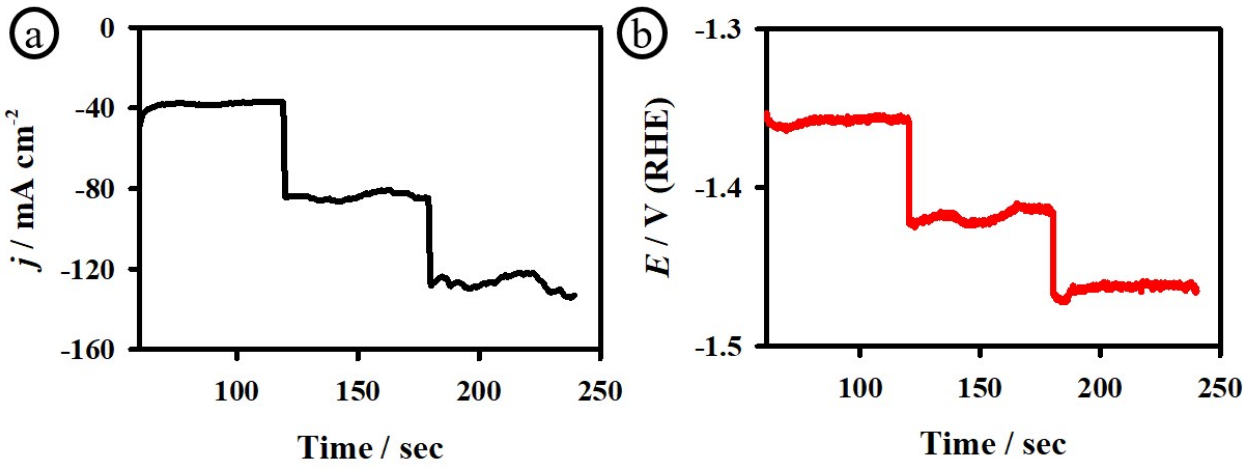


**Fig. S23.** CA response of the $Ni(OH)_2@Fe_xCo_{1-x}Pi|NiO$ heterostructures (black) electrode at different applied potentials of -1.35, -1.43 and -1.48 V vs. (RHE) (a). CP response of the $Ni(OH)_2@Fe_xCo_{1-x}Pi|NiO$ heterostructures (red) electrode at different applied current densities of -50, -100, and -150 mA $cm^{-2}$ (b).

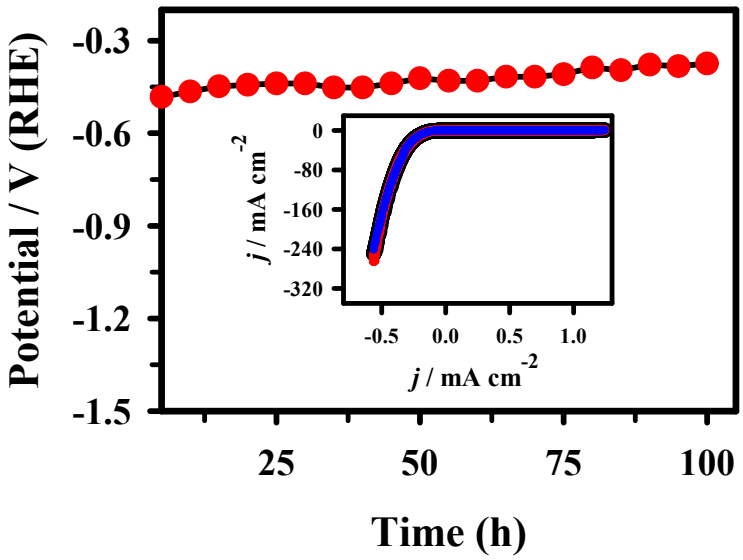


**Fig. S24.** Chronoamperometric response of the $Ni(OH)_2@Fe_xCo_{1-x}Pi|NiO$ heterostructures at the applied constant potential of ~ -0.17 V for 100 h. Inset: reproducible HER polarization curves of the three-type new $Ni(OH)_2@Fe_xCo_{1-x}Pi|NiO$ heterostructures recorded in 1.0 M KOH at a scan rate of 10 mV $s^{-1}$.

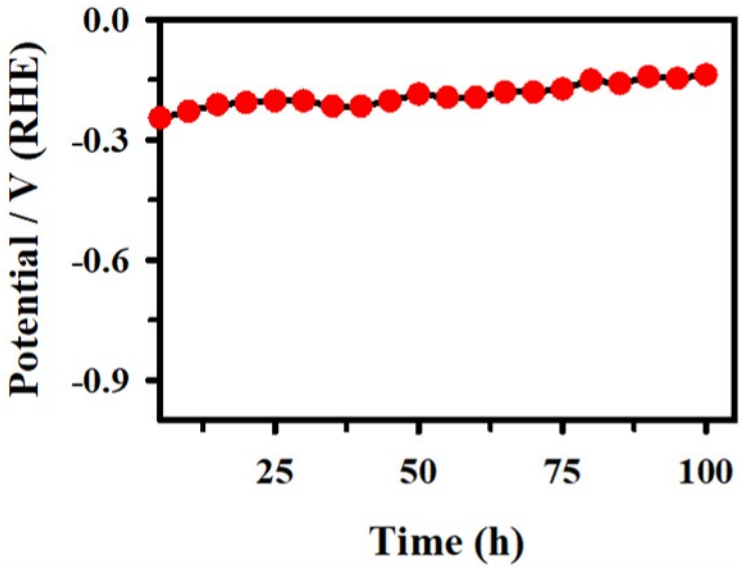


**Fig. S25.** Chronopotentiometric response of the $Ni(OH)_2@Fe_xCo_{1-x}Pi|NiO$ heterostructures at the applied constant current density of -10.0 mA $cm^{-2}$ for 100 h.

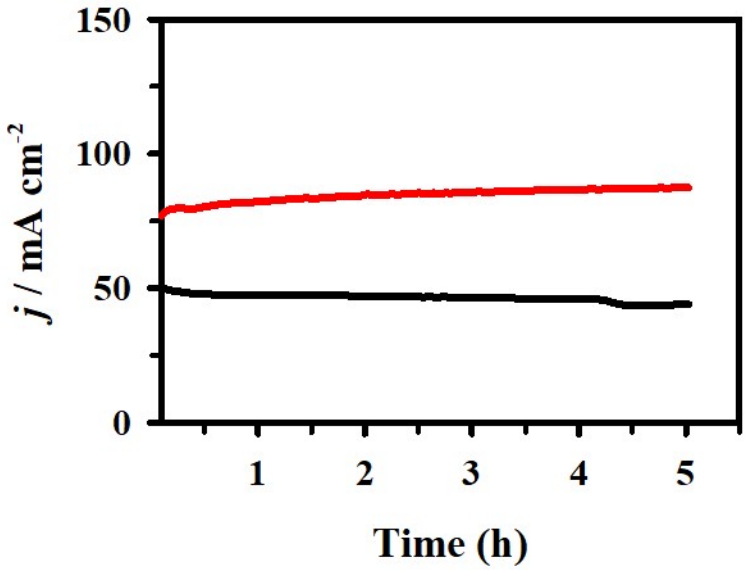


**Fig. S26.** CA curves of the $Ni(OH)_2@Fe_xCo_{1-x}Pi|NiO$ || $Ni(OH)_2@Fe_xCo_{1-x}Pi|NiO$ (red), and state-of-the-art commercial $IrO_2$ || Pt/C couple (black) electrodes for full water splitting. Electrolyte: 1.0 M KOH.

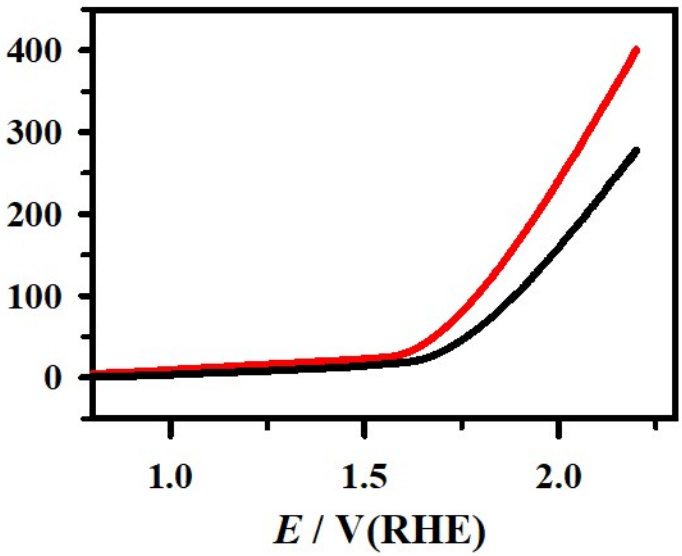


**Fig. S27.** LSV curves of the $Ni(OH)_2@Fe_xCo_{1-x}Pi|NiO$ || $Ni(OH)_2@Fe_xCo_{1-x}Pi|NiO$ (red), and $IrO_2$ || Pt/C couple (black) electrodes under 1.0 M KOH.

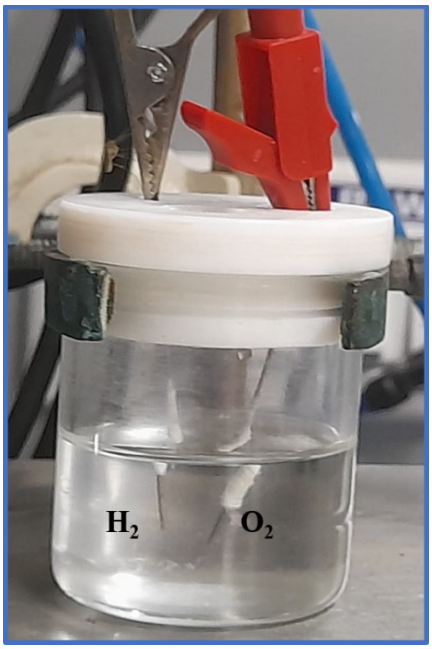


**Fig. S28**. Photograph of two-electrode cell setup based on $Ni(OH)_2@Fe_xCo_{1-x}Pi|NiO$ || $Ni(OH)_2@Fe_xCo_{1-x}Pi|NiO$ electrodes for the generation of $O_2$ and $H_2$. Electrolyte: 1.0 M KOH.

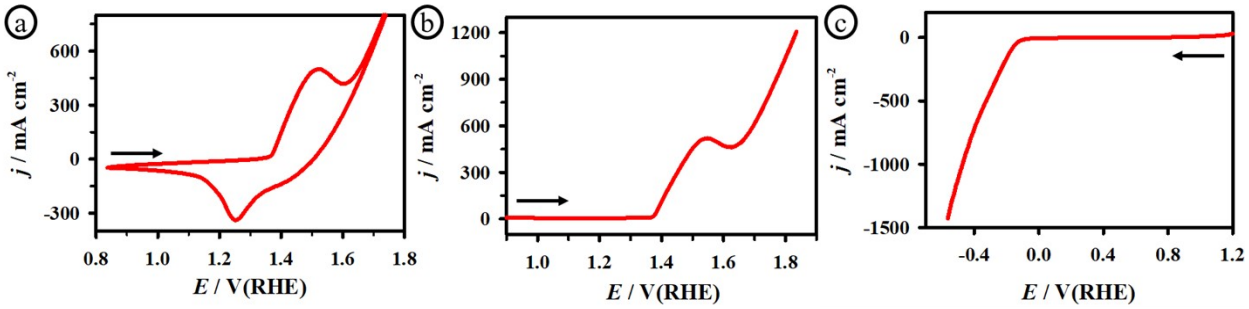


**Fig. S29**. CV (a), LSV OER (b) and HER (c) curves of the $Ni(OH)_2@Fe_xCo_{1-x}Pi|NiO$ heterostructures recorded in 1.0 KOH at the scan rate of 5.0 $mVs^{-1}$. (Surface area 2 x 2 cm).

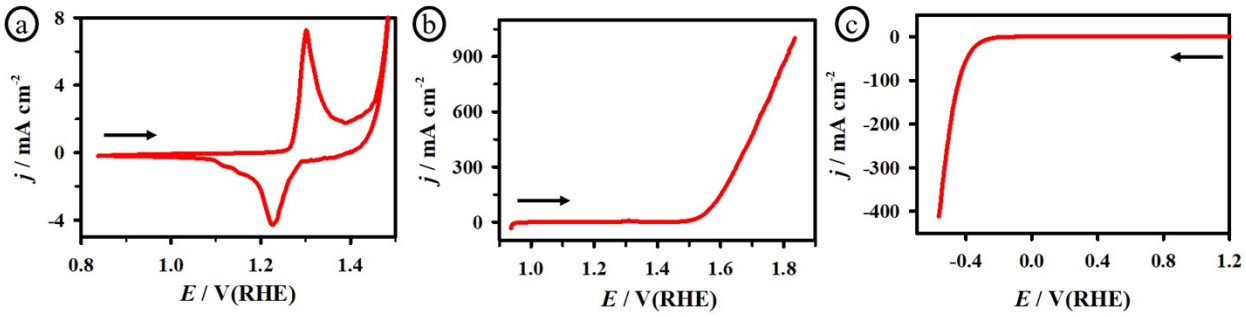


**Fig. S30**. CV (a), LSV OER (b) and HER (c) curves of the $Ni(OH)_2@Fe_xCo_{1-x}Pi|NiO$ heterostructures recorded in 30% KOH at the scan rate of 5.0 $mVs^{-1}$.

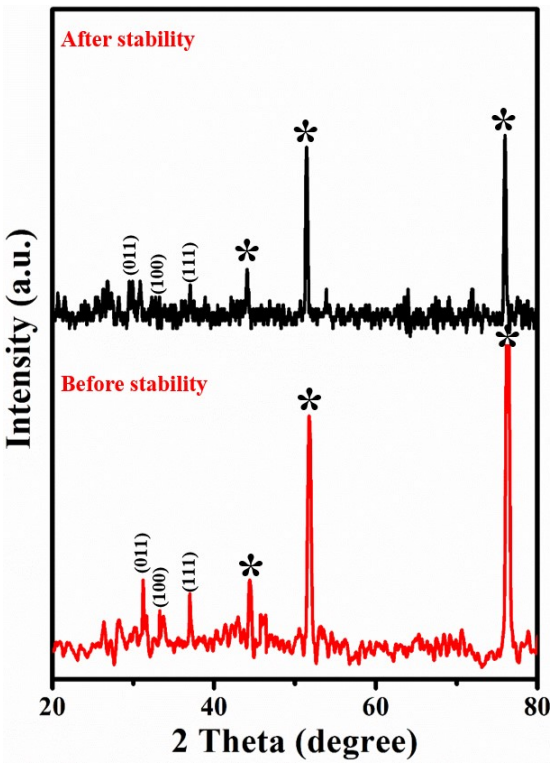


**Fig. S31.** XRD pattern of the $Ni(OH)_2@Fe_xCo_{1-x}Pi|NiO$ heterostructures prior to- (red), and after had a stability test (black).

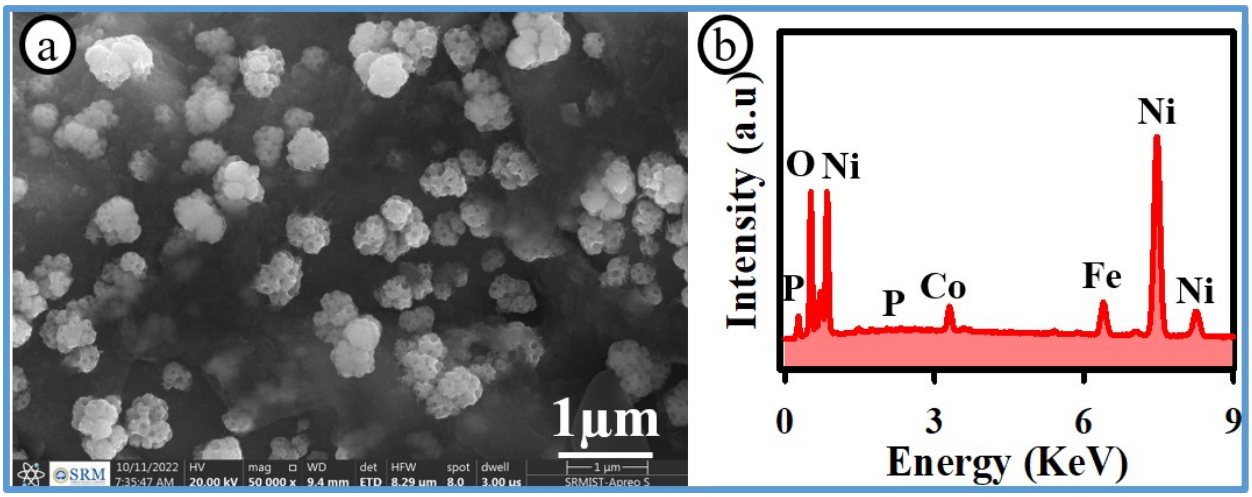


**Fig. S32.** HRSEM image (a), and EDX spectra (b) of the $Ni(OH)_2@Fe_xCo_{1-x}Pi|NiO$ heterostructures after long-term stability test.

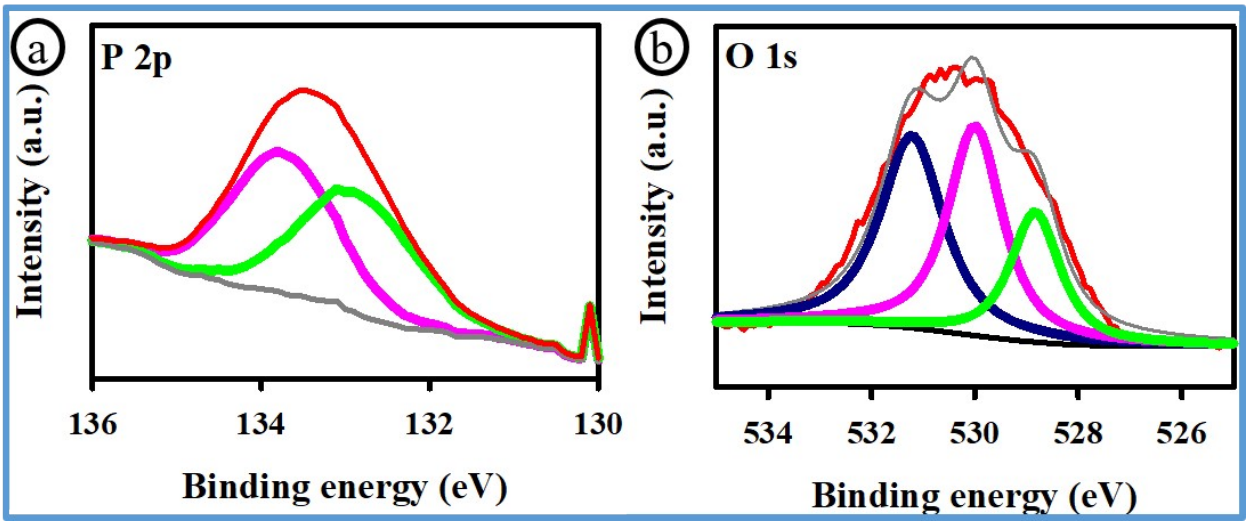


**Fig. S33.** XPS spectra P 2p (a), and O 1s (b) of the $Ni(OH)_2@Fe_xCo_{1-x}Pi|NiO$ heterostructures after long-term stability test.

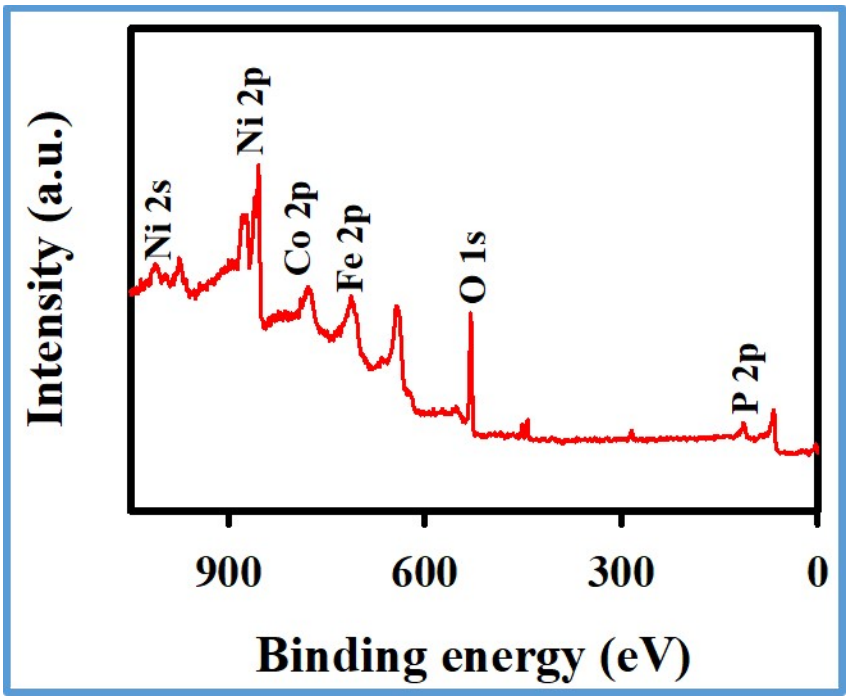


**Fig. S34.** XPS survey spectra of the $Ni(OH)_2@Fe_xCo_{1-x}Pi|NiO$ heterostructures after long-term stability test.

## References


S1 M. Arivazhagan and G. Maduraiveeran, *Materials Chemistry and Physics*, 2023, **295**, 127084.

S2 S. Marimuthu, A. Shankar and G. Maduraiveeran, *Chemical Communications*, 2023, **59**, 2600–2603.

S3 Z. Xing, L. Gan, J. Wang and X. Yang, *Journal of Materials Chemistry A*, 2017, **5**, 7744–7748.

S4 R. Elakkiya and G. Maduraiveeran, *Langmuir*, 2020, **36**, 4728–4736.

S5 A. Shankar and G. Maduraiveeran, *Journal of Electroanalytical Chemistry*, 2022, **923**, 116806.

S6 R. G. Jadhav, D. Singh, P. V. Krivoshapkin and A. K. Das, *Inorganic Chemistry*, 2020, **59**, 7469–7478.

S7 D. Duan, D. Guo, J. Gao, S. Liu and Y. Wang, *Journal of Colloid and Interface Science*, 2022, **622**, 250–260.

S8 X. Zhang, S. Zhu, L. Xia, C. Si, F. Qu and F. Qu, *Chemical Communications*, 2018, **54**, 1201–1204.

S9 X. Du, Z. Yang, Y. Li, Y. Gong and M. Zhao, *Journal of Materials Chemistry A*, 2018, **6**, 6938–6946.

S10 C. S. Saraj, S. C. Singh, A. Shukla, W. Yu, M. U. Fayyaz and C. Guo, *ChemElectroChem*, 2021, **8**, 209–217.

S11 H. Wang, C. Wang, W. Zhang and S. Yao, *International Journal of Hydrogen Energy*, 2022, **47**, 14916–14929.

S12 Y. Rao, Y. Wang, H. Ning, P. Li and M. Wu, *ACS Applied Materials & Interfaces*, 2016, **8**, 33601–33607.

S13 Y. Sang, X. Cao, L. Wang, G. Ding, Y. Wang, D. Yu, Y. Hao, L. Li and S. Peng, *International Journal of Hydrogen Energy*, 2020, **45**, 30601–30610.

S14 C. Chang, S. Zhu, X. Liu, Y. Chen, Y. Sun, Y. Tang, P. Wan and J. Pan, *Industrial & Engineering Chemistry Research*, 2021, **60**, 2070–2078.

S15 S. Liu, Y. Xing, Z. Zhou, Y. Yang, Y. Li, X. Xiao and C. Wang, *Journal of Materials Chemistry A*, 2023, **11**, 8330–8341.

S16 S. Marimuthu, A. Shankar and G. Maduraiveeran, *Energies*, 2023, **16**, 1124.